Journal of Geodesy (2024) 98:59
https://doi.org/10.1007/s00190-024-01872-z

ORIGINAL ARTICLE

Continental and oceanic AAM contributions to Chandler Wobble with the amplitude attenuation from 2012 to 2022

Xue-Qing Xu[1,2] · Ming Fang[1] · Yong-Hong Zhou[1,2] · Xin-Hao Liao[1,2]

Received: 12 July 2023 / Accepted: 29 May 2024 / Published online: 19 June 2024

Abstract
We reconstructed the Chandler Wobble (CW) from 1962 to 2022 by combining the Eigen-oscillator excited by geophysical fluids of atmospheric and oceanic angular momentums (AAM and OAM). The mass and motion terms for the AAM are further divided with respect to the land and ocean domains. Particular attention is placed on the time span from 2012 to 2022 in relation to the observable reduction in the amplitude of the CW. Our research indicates that the main contributor to the CW induced by AAM is the mass term (i.e., the pressure variations over land). Moreover, the phase of the AAM-induced CW remains relatively stable during the interval of 1962–2022. In contrast, the phase of the OAM-induced CW exhibits a periodic variation with a cycle of approximately 20 years. This cyclic variation would modulate the overall amplitude of the CW. The noticeable amplitude deduction over the past ten years can be attributed to the evolution of the CW driven by AAM and OAM, toward a state of cancellation. These findings further reveal that the variation in the phase difference between the CW forced by AAM and OAM, may be indicative of changes in the interaction between the solid Earth, atmosphere, and ocean.

Keywords Atmospheric angular momentum · Oceanic angular momentum · Chandler Wobble · Polar motion

1 Introduction

As the most significant Eigen-oscillator of the Earth, the Chandler Wobble (CW) is of great interest in astrogeodynamics and geophysics. Since frictional dissipation eventually dampens free oscillation, the alive CW suggests a continuous excitation. Various mechanisms for the CW excitation have been proposed in numerous studies, ranging from possible deep core motion to shallow earthquakes (Gibert and Le Mouël 2008; Smyliea et al. 2015; Bizouard 2020). By taking advantage of modern space technologies, high-quality atmospheric angular momentum (AAM) and reliable oceanic angular momentum (OAM) data have become available since the 1980s. Greater interest surrounding the effect of fluid source has occurred in recent years (Brzeziński and Nastula 2002; Gross et al. 2003; Zhou et al. 2005; Seitz and Schmidt 2005; Bizouard et al. 2011; Muskett 2021).

Numerous studies have been conducted to examine the impact of regional AAM on the excitations of polar motion (Nastula and Salstein 1999; Nastula et al. 2009, 2014), wherein notable investigations have revealed a general resemblance between the regional contributions and the global excitations of polar motion. Zotov and Bizouard (2015) investigated the impact of regional atmospheric factors on the CW. They found a pattern of the CW that exhibited an inverse relationship with the AAM, with this pattern emerging over a period of approximately 20 years in both the Northern and Southern hemispheres. In contrast to the approach taken by Nastula et al. (2009) as well as Zotov and Bizouard (2015), who estimated the contributions of high-resolution regional sectors to the AAM, our study focuses solely on differentiating the AAM between continental and oceanic regions (in this paper, the continental and oceanic

✉ Xue-Qing Xu
xqxu@shao.ac.cn

Ming Fang
fang@chandler.mit.edu

Yong-Hong Zhou
yhzhou@shao.ac.cn

Xin-Hao Liao
xhliao@shao.ac.cn

[1] Shanghai Astronomical Observatory, Chinese Academy of Sciences, Shanghai 200030, China

[2] Key Laboratory of Planetary Sciences, Chinese Academy of Sciences, Shanghai 200030, China

AAM refer to the AAM over the land and ocean, respectively). In addition, the AAM is further divided into mass and motion terms. It was found that the CW resulting from the continental AAM-motion exhibits an inverse relationship with the CW generated by the oceanic AAM-motion. Additionally, the contribution of the oceanic AAM-mass term is approximately ten times smaller than that of the continental AAM-mass term. These two events result in the AAM-mass over the land becoming the main trigger of CW generated by AAM.

Previous investigations have identified anomalies of the CW in the 2010s, with changes in atmospheric excitation suggested to be the likely reason (Wang et al. 2016; Zotov et al. 2022; Malkin 2023; Yamaguchi and Furuya 2024). In this study, we explored deeper into the factors contributing to the reduction in the CW amplitude. Specifically, we examined the relationship between the global AAM and OAM, aiming to understand their coupling mechanism. In order to achieve this objective, we undertook the task of reconstructing the CW series composing a decaying Eigen-oscillator and the effect of the AAM and OAM excitations. This approach was grounded on the theoretical framework of polar motion. In the process of reconstruction, two distinct datasets of AAM and OAM obtained from different coupled models are employed. The comparative results demonstrate that the two modeled CW align closely with the observed CW, exhibiting high correlation coefficients ranging from 0.96 to 0.98. In general, the excitation modes induced by the global AAM and OAM show distinct characteristics. Specifically, the AAM tends to amplify the amplitudes of the CW, while the OAM serves to modulate the amplitudes of the CW. The noticeable reduction in the amplitude of the CW over the past ten years, can be attributed to the nearly antiphase relationship, between the AAM-induced polar motion and OAM-induced one. This finding provides additional evidence of the change in the dynamics of the interaction between the solid Earth, atmosphere, and ocean over the past decade.

2 Data and methods

2.1 Data series

In this study, the CW observations are extracted from the IERS EOP 14 C04 polar motion series that comes from the International Earth Rotation and Reference Systems Service (IERS) (Gambis 2004; Bizouard et al. 2019). The AAM series that are divided into separate components are derived using data from the National Center for Environmental Prediction/National Center for Atmospheric Research (NCEP/NCAR) reanalysis data set R1 (see Sect. 2.3 for more details) (Salstein et al. 1993; Kalnay et al. 1996); and the coupled OAM data are obtained from the Estimating the Circulation and Climate of the Ocean (ECCO) (Gross 2009). For comparison, the geophysical fluids of AAM and OAM from the Earth System Modeling GeoForschungsZentrum in Potsdam (ESMGFZ) are also employed (Dobslaw and Dill 2018; Dill et al. 2019). It is important to acknowledge that the ESMGFZ AAM and OAM series are derived from the 3 h European Center for Medium Weather Forecasting (ECMWF) operational data.

Table 1 Datasets employed in this study

Model/dataset	Products	Time span
IERS EOP 14 C04	polar motion	1962–2022
NCEP	AAM	1948–2022
ECCO	OAM	1949–2018
ESMGFZ	AAM and OAM	1976–2022

Table 1 presents the model products and data availability spans derived from the aforementioned sources. In order to maintain consistency with the CW observations, the geophysical fluid datasets are firstly reduced or interpolated to daily mean series. In the context of the CW reconstruction utilizing the coupled NCEP–ECCO data, the CW, AAM and OAM are examined within the shared time frame of 1962–2018. Additionally, the three datasets are selected for the period spanning from 1976 to 2022, with the purpose of employing the ESMGFZ AAM/OAM data.

2.2 Theoretical framework of polar motion

The Liouville differential equation is transformed from the instantaneous rotation pole m to the observed pole coordinates of the Celestial Intermediate Pole (CIP) p. It involves the effective excitation function. In this work, arc-second (as) is the unit of both functions and observations and that Liouville equation takes the form (Bizouard 2020; Gross 1992)

$$\begin{cases} \frac{i}{\sigma_c}\frac{\mathrm{d}p(t)}{\mathrm{d}t} + p(t) = \chi(t), \\ \sigma_c = \frac{2\pi}{T_c}\left(1 + \frac{i}{2Q_c}\right). \end{cases} \tag{1}$$

The effective excitation function is given by

$$\chi = (\alpha_1 \Omega \Delta I + \alpha_2 h)/[\Omega(C - A)], \tag{2}$$

where Ω is the Earth average spin rate, A and C are the equatorial and the axial moment of inertia, ΔI is perturbation term of the Earth's inertia tensor and also called as the mass term, h is the relative angular momentum and is also named as the motion term. The factors $\alpha_1 = 1.101$, $\alpha_2 = 1.610$ summarizing all those various effects (such as loading deformation and anelasticity) are retained from the

ESMGFZ datasets, and these values are also employed in calculations with the NCEP–ECCO data (Dobslaw and Dill 2018). σ_c is the complex Chandler frequency, here, values of the observed Chandler period $T_c = 432.5 \pm 0.8d$ and quality factor $Q_c = 69 \pm 22$ were re-estimated, by employing the method suggested by Wilson and Vicente (1990).

Starting from the fixed epoch t_0 of arbitrary choice, we can simplify the polar motion solution as

$$p(t) = p(t_0)e^{i\sigma_c(t-t_0)} - i\sigma_c \int_{t_0}^{t} e^{i\sigma_c(t-t')}\chi(t')\mathrm{d}t', \tag{3}$$

where $p(t_0)$ is a constant complex amplitude of the polar motion observation at epoch t_0.

The CW is a part of the polar motion that corresponds exclusively to the irregular fluctuations of the surface fluid (Fang et al. 2021, 2022). Here, we just consider contributions from AAM and OAM, thus, the excitation can be symbolically written as

$$\chi = \chi_{\mathrm{AAM}} + \chi_{\mathrm{OAM}}. \tag{4}$$

We can see from the solution (3) and the symbolic expression (4) that the polar motion or the CW reconstructed in this paper is composed of three separate components: (i) a decaying Eigen-oscillator $p(t_0)e^{i\sigma_c(t-t_0)}$; (ii) a forced term by the atmosphere expressed by the AAM integration; (iii) a forced term by the ocean expressed by the OAM integration.

2.3 Calculations of the continental and oceanic AAM

The expressions for the equatorial AAM, split up into the pressure (mass) and wind (motion) terms, are as follows:

$$L^{\mathrm{p}} = L_1^p + iL_2^p = \frac{-\Omega R^4}{g}\iint P_s \sin\varphi\cos^2\varphi e^{i\lambda}\mathrm{d}\lambda\mathrm{d}\varphi, \tag{5}$$

$$L^{\mathrm{w}} = L_1^{uv} + iL_2^{uv} = \frac{-R^3}{g}\iiint (u\sin\varphi + iv)\cos\varphi e^{i\lambda}\mathrm{d}p\mathrm{d}\lambda\mathrm{d}\varphi, \tag{6}$$

where p_s is the surface atmospheric pressure, u, v are the zonal and meridional wind velocities, respectively, R is the radius of the Earth,g is the gravitational acceleration, λ is longitude, and φ is latitude. The surface atmospheric pressure as well as the zonal and meridional wind velocities data used in Eqs. (5) and (6) were obtained from the NCEP/NCAR reanalysis data set R1. First, we estimated the global and the oceanic AAM, then the continental AAM was deduced by forming the difference between the global and the oceanic AAM. Similar to the approach employed in the ESMGFZ AAM series, here we applied the inverted barometer correction for calculating the decomposed AAM. The estimates pertaining to the equatorial AAM represented in this research are in agreement with those of the axial component. For more elaboration, we suggest referring to our previously published work (Xu et al. 2022).

According to the theoretical framework of polar motion discussed in Sect. 2.2, the geophysical fluid excitations can be calculated by Eq. (2); then, the forced polar motion can be calculated from the excitation series by Eq. (3), wherein the CW is contained. The AAM excitations over the land and over the ocean are compared in Fig. 1. There, the contribution of wind to the AAM, denoted by AAM-motion, is separated from the contribution of the atmospheric mass redistribution, denoted by AAM-mass.

From Fig. 1, we conclude that the oceanic AAM-mass excitation (light blue lines in panels (a)&(b)) is one order of magnitude smaller than the continental AAM-mass excitation (orange lines in panels (a)&(b)). Prior studies have also demonstrated a comparable outcome (Nastula et al. 2009; Zotov and Bizouard 2015), which can be attributed in part to the equilibrium between atmospheric mass transfer over the ocean and evaporation precipitation cycles. Moreover, the magnitudes of the land and ocean AAM-motion excitation are about 2–3 times larger than those of the continental AAM-mass excitation. But, the global AAM-motion excitation is about 2–3 times smaller than the global AAM-mass term. That weakness of the AAM-motion term results from the global destructive interference between the land contribution (purple lines in panels (c) & (d)) and ocean contribution (green lines in panels (c) & (d)). This cancellation may reveal the general atmospheric circulation mode between the lands and the ocean.

3 Results

3.1 Continental and oceanic AAM contributions to CW

First, we reconstructed the polar motion induced by AAM or OAM excitations according to Eq. (3). Then, we excluded fluctuations beyond 2 years by applying a high-frequency pass Butterworth filter to the calculated polar motions. For further information on decreasing the edge effect induced by filtering, we recommend referring to our previously published work (Xu et al. 2022). After that, the seasonal patterns (such as the annual and semi-annual variations) were fitted and removed to retain the tiny fluctuations in the CW amplitude. The extracted CW from polar motion observations is obtained in a manner similar to the modeled CW. To distinguish between different CW signals, in this paper, the CW extracted from polar motion calculations integrated singly from the AAM and OAM excitation are referred to as the AAM-induced CW and OAM-induced CW, respectively, whereas the CW extracted from polar motion observations

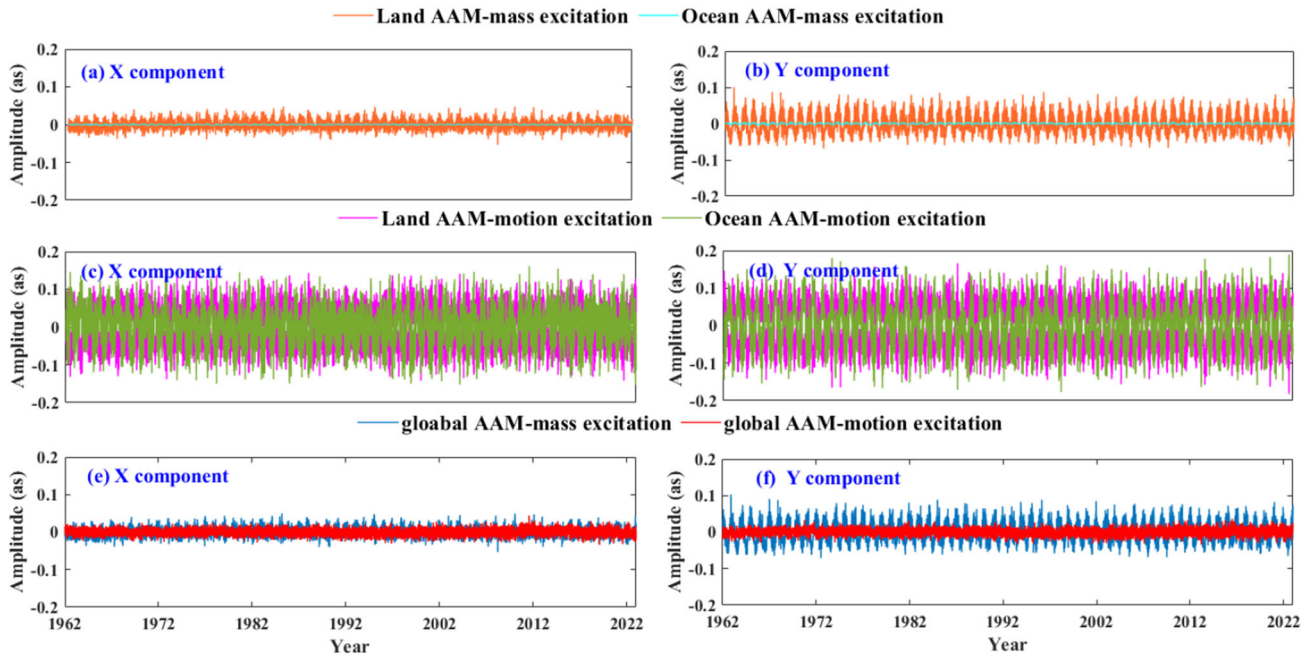

Fig. 1 Time series of the AAM excitation from 1962 to 2022, with the mass and motion terms calculated separately over the land, ocean, and entire globe. **a** & **b** show X (left plots) and Y (right plots) components of the AAM-mass excitation over the land and ocean; **c** & **d** present X and Y components of AAM-motion excitation over the land and ocean; while X and Y components of the AAM-mass and -motion excitation over the globe are displayed in **(e)** & **(f)**

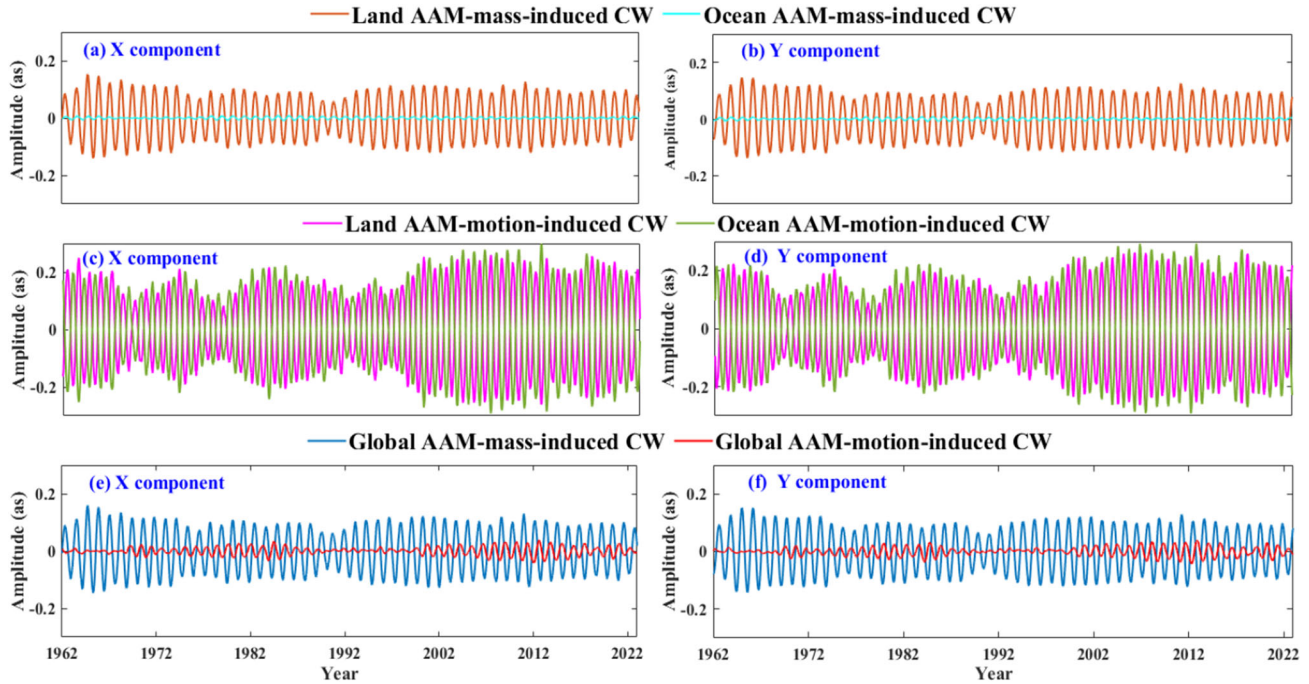

Fig. 2 Time series of the AAM-induced CW from 1962 to 2022, with the mass and motion terms calculated separately over the land, ocean, and entire globe. **a** & **b** display X (left plots) and Y (right plots) components of the CW generated by AAM-mass over the land and ocean; **c** & **d** present two components of the CW derived by AAM-motion over the land and ocean; X and Y components of the CW forced by AAM-mass and -motion over the globe are performed in **(e)** & **(f)**

are identified as the observed CW. The integrated CW signals resulting from the decomposed AAM excitations are shown in Fig. 2.

As the AAM-mass excitation over the ocean is much smaller than all other atmospheric excitation components (land AAM-mass, land AAM-motion, ocean AAM-motion, see Fig. 1), it is not surprising to observe that feature in the corresponding CW effects (see Fig. 2). In addition, the CW induced by AAM-motion over the land (purple lines in panels (c)&(d)) is generally anti-correlated with the one induced over the ocean (green lines in panels (c)&(d)). As a result, the land–ocean cancellation reduces the overall contribution of AAM-motion to the CW (red lines in panels (e)&(f)). Actually, such a cancellation had been detected in the AAM-motion excitation displayed in Fig. 1. This land–ocean cancellation may be partly caused by the anti-correlated patterns of the atmospheric activities in the Northern and Southern hemispheres, as identified by Zotov and Bizouard (2015).

Furthermore, as the AAM-mass over the ocean can be ignored, and AAM-motion is strongly reduced by land–ocean out-of-phase regime, the principal contributor to CW is the AAM-mass term (blue lines in panels (e)&(f)). Hereafter, the term "AAM-mass" should be understood as AAM-mass over the land. This finding contrasts with the case of the axial component, where the AAM-motion term over the ocean is dominant (Xu et al. 2022).

3.2 Reconstruction of the CW

Based on the theoretical description of polar motion given in Sect. 2.2, we calculated the CW signal by combing three components: (i) the decaying Eigen-oscillator with a time variable displaced by $t - t_0$, $t_0 = 1962.0$; (ii) the CW induced by AAM; (iii) the CW caused by OAM. The sum of these three parts can be abbreviated as the combined CW or modeled CW. The combined CW is expected to recover the observed CW signal, and this is certainly confirmed in Fig. 3, which shows the results obtained using AAM + OAM from the coupled NCEP-ECCO datasets. For compassion, the separated CW induced by AAM and OAM from the ESMGFZ, as well as the combined CW are estimated in Fig. 4. Here, the initial time of the decaying Eigen-oscillator is chosen at $t_0 = 1976.0$. In order to evaluate the impact of AAM + OAM excitations on CW, we have calculated a list of correlation coefficients between the observed CW and the modeled CW from various datasets. This analysis was conducted both with and without taking into account the decaying Eigen-oscillator. The results are presented in Table 2. All cross-correlations in this study are evaluated with a 99% significance level, as reported by Zhou and Zheng in 1999.

Three notable characteristics are derived from the similar calculations in Figs. 3 and 4, as well as from Table 2. First, the two modeled CW (red dash lines in panels (c)&(d)) derived from different AAM + OAM datasets exhibit strong agreement with the observed CW (black lines in panels (c)&(d)). The coefficients obtained from combining the Eigen-oscillator and the data series after removing the Eigen-oscillator, both fall within narrow ranges of 0.96–0.98 and 0.92–0.95. Previous researches have also reached a similar conclusion, highlighting the significant contributions of AAM + OAM to CW signal (Bizouard et al. 2011; Zotov and Bizouard 2016). In addition, the slight differences between the observed CW and the CW calculated by fluid excitations can be attributed to other minor factors including the inaccuracies in AAM + OAM estimations.

Second, as the separated CW signals shown in panels (a)&(b) of Fig. 3, the AAM-induced CW (green dash lines) is almost in-phase with the decaying Eigen-oscillator (pink lines), causing the CW's amplitude to increase. On the other hand, the phase of the OAM-induced CW (blue lines) undergoes a cycle of approximately 20 years, with the AAM-induced CW serving as a reference. The black dash lines indicate the time periods of in-phase and out-of-phase. During the period of in-phase, the CW experienced modulation resulting in larger amplitude fluctuations (~ 0.2 *as* from 1982 to 2002). In contrast, during the period of out-of-phase, the CW amplitudes were smaller in magnitude (~ 0.15 *as* from 1962 to 1982 and ~ 0.1 *as* from 2002 to 2018). The atmospheric-forced CW has a comparable pattern in both the Northern and Southern hemispheres (Zotov and Bizouard 2015; Zotov et al. 2022). This pattern is also observed in significant climate events and requires additional research to be conducted (Xu et al. 2023).

Furthermore, Fig. 4 demonstrates comparable outcomes when utilizing the CW derived from ESMGFZ records. For more comprehensive information regarding the attenuation from 2012 to 2022 (shown by the yellow shading), please refer to panels (c)&(d). This anomalies in CW have been recognized in previous studies and will be further examined in Sect. 3.4. Despite two successful reconstructions of the CW, it is important to acknowledge that the magnitudes of the Eigen-oscillator and the decomposed CW induced by AAM and OAM as depicted in Fig. 4, perform differently somewhat from those of the three components displayed in Fig. 3. This discrepancy can be attributed to the distinct initial epochs of 1962 and 1976.

3.3 Deconvolution of observed CW

To investigate the excitation mechanism of the CW, we performed a deconvolution of the previously extracted CW by employing polar motion data and exhibited the total excitations in Fig. 5 (Clark 1985). Subsequently, the NCEP-ECCO

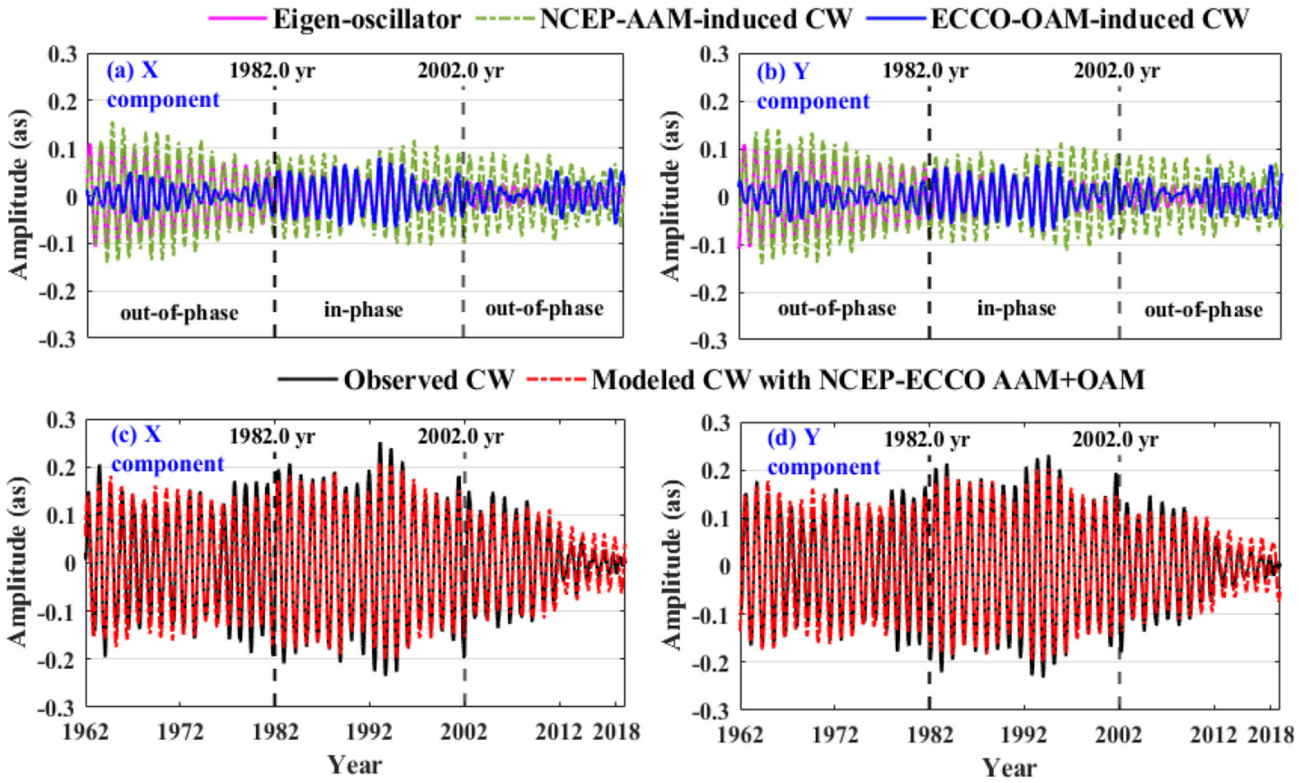

Fig. 3 Time series of the CW modeled from the NCEP-ECCO AAM + OAM as well as the combined and observed CW from 1962 to 2018, the dash black lines mark the time spans of in-phase and out-of-phase between the CW induced by AAM and OAM. **a** & **b** show X (left plots) and Y (right plots) components of the Eigen-oscillator, CW induced by AAM and OAM; **c** & **d** present X and Y components of the observed CW and combined CW

and ESMGFZ datasets were compared to the deconvolution series, specifically focusing on the AAM + OAM excitations. In this analysis, the annual and semi-annual terms in both sets of AAM + OAM excitations were excluded.

The deconvolution of the observed CW signal, represented by the black lines in panels (a) and (b), demonstrates a strong agreement with the AAM + OAM excitations from different models, as indicated by the red dashed and blue dotted lines. The average correlation coefficient between the deconvolution of the observed CW and the two sets of AAM + OAM excitations was determined to be $\sim 0.885 \pm 0.018$. This statistical calculation has excluded the 1983–1993 time period because of notable observational error noise in the black lines. The coefficient closely approximates the value of the convoluted series presented in Table 2, reaffirming the prominent influence of AAM + OAM excitations in the CW signal. The Fourier power spectrum in panel (c) of the deconvoluted series indicate that the CW signal extracted in this paper is highly efficient, with most of the extraneous influences (such as the long-terms and seasonal variations) being largely eliminated. Furthermore, the distributions of the three spectra exhibit consistency in the primary frequency bands, but with discernible variations in specific aspects. The specific discrepancies in the spectra can also be ascribed to other minuscule factors, in addition to inaccuracies in modeling the global AAM and OAM. The spectral distributions in the vicinity of the Chandler frequency exhibit low intensity in all excitation series, indicating a weak resonance power at the Chandler frequency.

3.4 Attenuation of the CW from 2012 to 2022

The remarkable occurrence of CW attenuation from 2012 to 2022, almost leading to its complete disappearance, warrants particular focus. In this study, our main focus was on the modeled CW and its various decompositions over the past ten years. Figure 6 shows the observed and modeled CW series. Because there was a shortage of ECCO-OAM after 2019 (Table 1), we only presented the CW signal estimated with the AAM + OAM from ESMGFZ. In order to further investigate the reasons for the attenuation of the CW, we compared the decomposed Eigen-oscillator and the CW induced by AAM and OAM, as well as other combinations

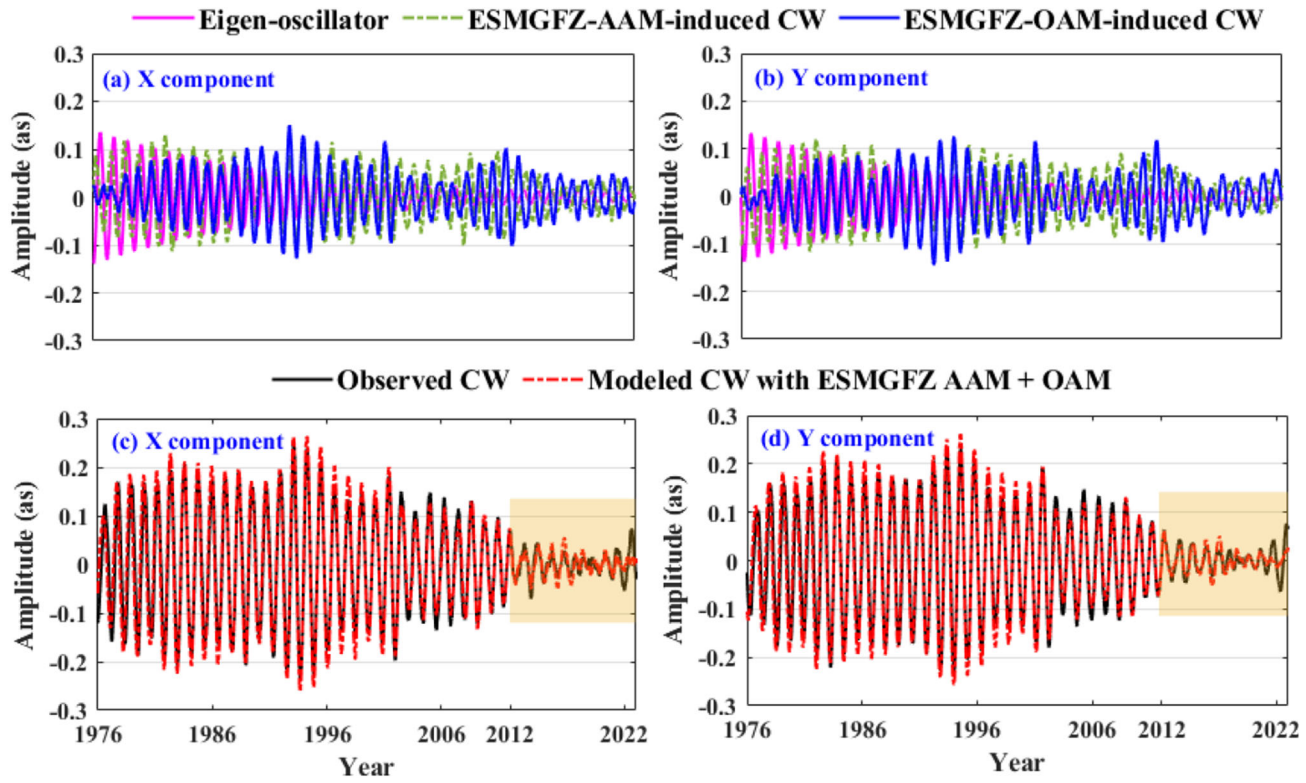

Fig. 4 Time series of the CW modeled from the ESMGFZ AAM + OAM as well as the combined and observed CW from 1976 to 2022, the yellow shading marks the period when the 2012–2022 attenuation occurred. **a** & **b** show X (left plots) and Y (right plots) components of the Eigen-oscillator, CW induced by AAM and OAM; **c** & **d** present X and Y components of the observed CW and combined CW

Table 2 Correlations between the observed CW and the CW modeled from different datasets, conducted both with and without taking into account the decaying Eigen-oscillator

	Time spans of 1962–2018		Time spans of 1976–2022	
Observed CW	Eigen-oscillator + (AAM + OAM)-induced CW of NCEP-ECCO		Eigen-oscillator + (AAM + OAM)-induced CW of ESMGFZ	
	X component	Y component	X component	Y component
	0.96 4 ± 0.003	0.967 ±0.003	0.97 5 ± 0.003	0.978 ±0.003
Observed CW with the Eigen-oscillator been removed	AAM + OAM-induced CW of NCEP-ECCO		AAM + OAM-induced CW of ESMGFZ	
	X component	Y component	X component	Y component
	0.92 4 ± 0.003	0.930 ± 0.003	0.94 6 ± 0.003	0.94 9 ± 0.003

of these three components in Fig. 7. In addition, the correlation coefficients between the observed CW and the various combinations are calculated and presented in Table 3.

Figure 6 illustrates a decline in the amplitudes of the CW over the past decade, followed by a projected increase until 2022. The magnitudes observed during the period of 1982–2002, as depicted in Fig. 3, were approximately four times larger (~ 0.2 *as*) compared to the current magnitudes (~ 0.05 *as*).

The decomposition analysis of the CW signals induced by the ESMGFZ AAM and OAM, as shown in Fig. 7, provides insight into the reason for the decline in CW. It is observed that throughout the period from 2012 to 2022, the OAM-induced CW (represented by green lines in panels (a)&(b)) becomes nearly inversely associated with the AAM-induced

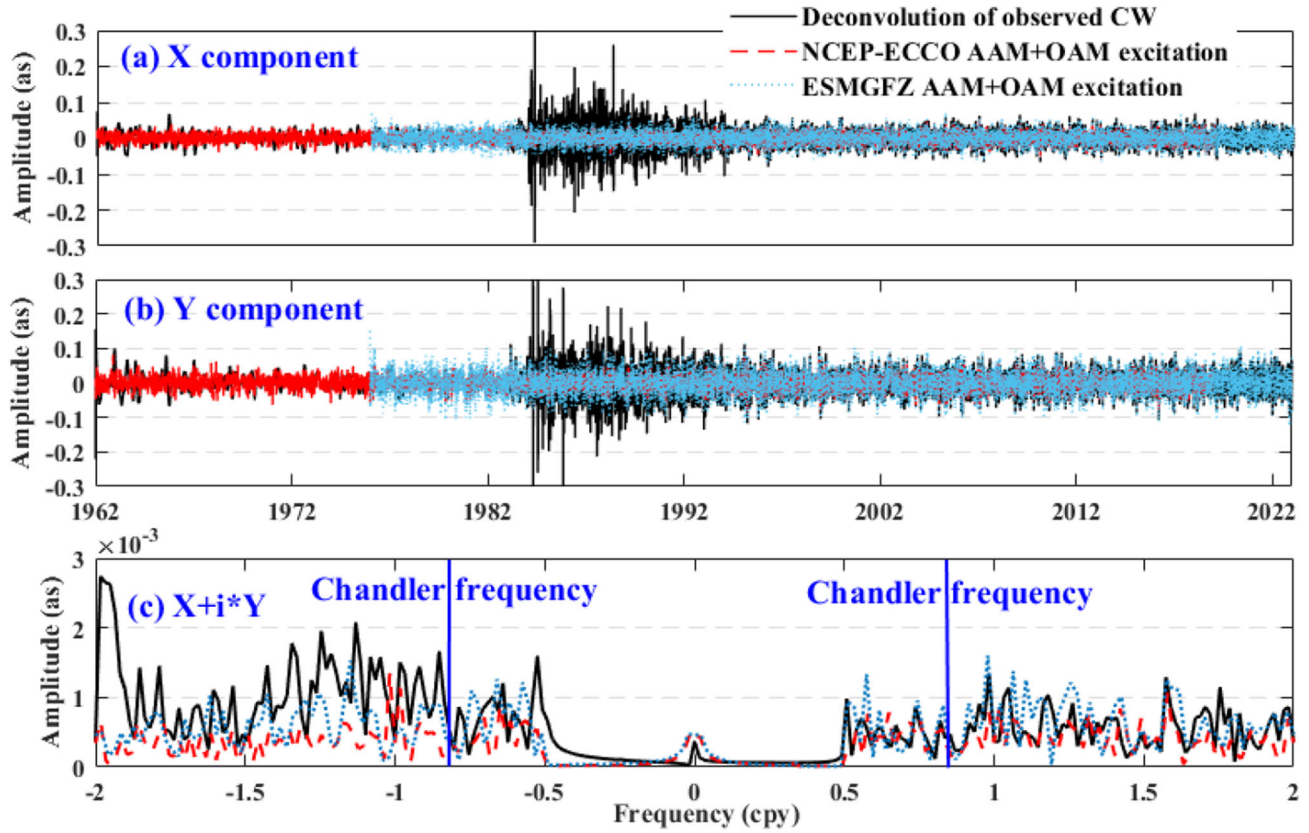

Fig. 5 Time series and Fourier power spectra of the de-convoluted CW as well as the AAM + OAM excitation from NCEP-ECCO and ESMGFZ. **a** & **b** show X and Y components of the deconvolution derived from the observed CW and of the two AAM + OAM excitation; **c** presents the complex Fourier power spectra of the de-convoluted CW and the two AAM + OAM excitation

CW (represented by blue lines). More precisely, the attenuation of the CW is caused by the cancellation between the CW generated by OAM and the Eigen-oscillator, combined with the CW induced by AAM (shown by pink lines in panels (c)&(d)).

The same outcome can be inferred from Table 3. Specifically, the coefficient between the observed CW and the Eigen-oscillator + AAM-induced CW is ~ 0.4. When the OAM-induced CW is added, the correlation increases to ~ 0.7, surpassing the correlation coefficients of other situations involving a single Eigen-oscillator (~ 0.5) and AAM + OAM-induced CW (~ 0.5). The correlations between the observed and modeled CW here (0.725 and 0.733) are lower compared to those estimated in Table 2 (0.975 and 0.978). This discrepancy is mostly due to larger relative differences between reconstructed and observed CW throughout the attenuation period of 2012–2022. In summary, the contrasting phase relationship between the CW induced by OAM and AAM indicates that the interaction regime between the solid Earth, atmosphere and ocean have undergone a significant shift in the past ten years. This shift appears to be manifested in a broader modulation pattern with a 20-year cycle.

4 Discussion and conclusion

We utilized the geophysical fluid datasets from two coupled models, namely NCEP-ECCO and ESMGFZ (as shown in Table 1), to reconstruct the CW fluctuations. This reconstruction was done using the theoretical framework of polar motion, as described in Sect. 2.2. The AAM excitation over the land is estimated separately from that over the ocean (as seen in Fig. 1). The decomposed result illustrates that the contribution of the AAM to the CW primarily originates from the AAM-mass over the land (as depicted in Fig. 2). Compared to the CW signals extracted from polar motion observations, both the two reconstructions demonstrate satisfactory performances (as shown in Figs. 3 and 4). The correlation coefficients for both reconstructions are higher than 0.95 (as indicated in Table 2). The deconvoluted series similarly displays comparable findings (Fig. 5).

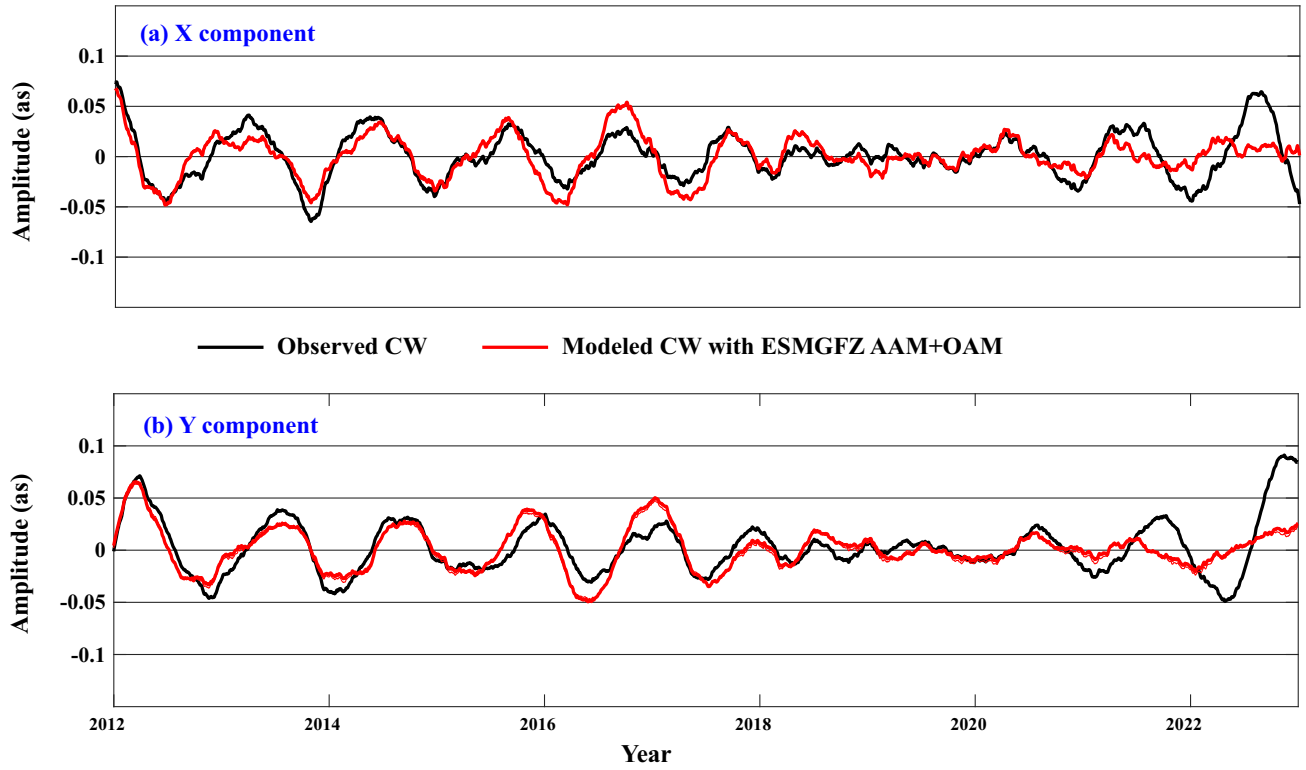

Fig. 6 Time series of the observed CW and CW modeled using the ESMGFZ AAM + OAM datasets during time period of 2012–2022. **a** X component; **b** Y component

The AAM is primarily derived from actual observations, with some further refinement through model computations. Conversely, the OAM is mainly based on model calculations, with limited input from few direct observations. The primary determinant for the model calculates of ocean circulation is the observed wind field. The successful restoration of the observed CW using the combined AAM and OAM provides strong evidence for the accuracy of the ocean circulation model.

During the analysis of the Eigen-oscillator and the CW forced by AAM and OAM, we found that the AAM-induced CW is almost in-phase with the Eigen-oscillator. On the other hand, the phase of OAM-induced CW changes periodically every ~ 20 years. This leads to variations in the amplitude of the CW, with periods of in-phase resulting in an increase, and periods of out-of-phase resulting in a decrease, respectively (as shown in Figs. 3 and 4). In addition, in order to investigate the reasons for the decline in CW from 2012 to 2022, we analyzed the combined and decomposed CW fluctuations in the past decade (Figs. 6 and 7). We also recalculated the correlation coefficients between the observed CW and other combinations (Table 3). The results indicate that the AAM-induced CW are still in-phase with the Eigen-oscillator, while the OAM-induced CW evolve to a totally antiphase with the Eigen-oscillator. The decrease in the CW over the past decade can be attributed to the cancellation between the OAM-induced CW and the combined effect of the Eigen-oscillator and the AAM-induced CW.

In summary, the alteration in the phase difference between the CW induced by the AAM-mass and the CW forced by the OAM could be ascribed to a worldwide shift in the climate regime. The ~ 20-year period illustrated in this phase difference may indicate a recurring climate change cycle, which requires further analysis and discussion. The decrease in CW amplitude during the past decade further suggests a shift in the interaction dynamics between the solid Earth, atmosphere and ocean. The correlation between recent extreme weather events and the decline in the CW is deserving of thorough investigation in the next years. Aside from the impacts of AAM and OAM on the excitation to the CW, there are additional minor factors, such as hydrologic angular momentum (HAM) and interior Earth excitation, that necessitate further examination.

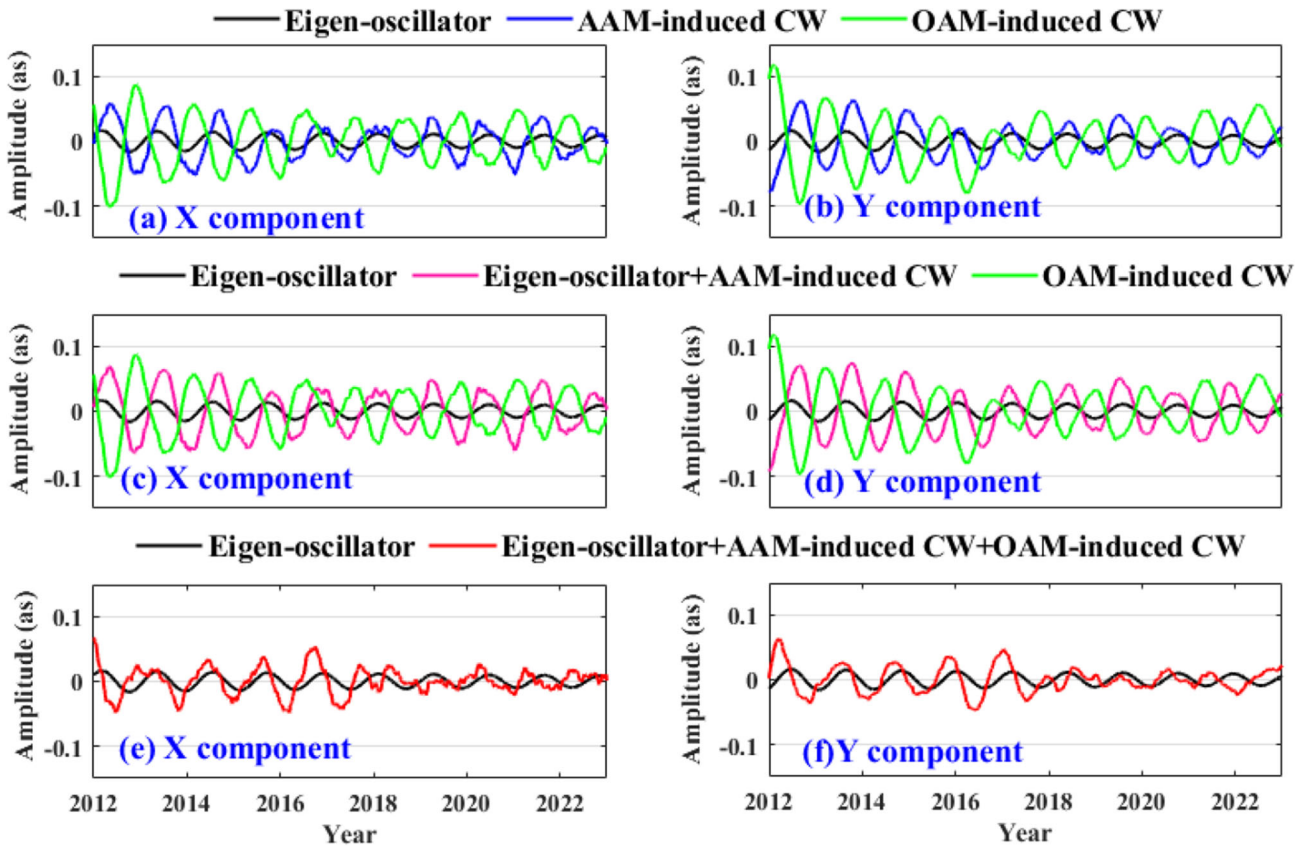

Fig. 7 Time series of the decomposed Eigen-oscillator, CW forced by the ESMGFZ AAM and OAM datasets, as well as the different combinations during time interval of 2012–2022. **a** & **b** show X (left plots) and Y (right plots) components of the three decomposed series; **c** & **d** present X and Y components of the Eigen-oscillator, Eigen-oscillator + AAM-induced CW and OAM-induced CW; **e** & **f** display X and Y components of the Eigen-oscillator and Eigen-oscillator + (AAM + OAM)-induced CW

Table 3 Correlation coefficients between the observed CW and the different combinations of Eigen-oscillator, CW induced by the ESMGFZ AAM and OAM datasets

	Observed CW	
	Time period of 2012–2022	
	X component	Y component
(AAM + OAM)-induced CW	0.52 2 ± 0.003	0.52 5 ± 0.003
Eigen-oscillator	0.51 4 ± 0.003	0.51 7 ± 0.003
Eigen-oscillator + AAM-induced CW	0.37 6 ± 0.003	0.41 2 ± 0.003
Eigen-oscillator + (AAM + OAM)-induced CW	0.72 5 ± 0.003	0.73 3 ± 0.003

Acknowledgments The authors thank the associate editor and all the reviewers for their great efforts. We also thank the IERS for providing the polar motion observations; the NCEP/NCAR for providing the AAM reanalysis data, and the ECCO for the OAM series; another AAM+OAM series are from the ESMGFZ. This work is supported by the B-type Strategic Priority Program of the Chinese Academy of Sciences (Grant No. XDB41000000), the National Natural Science Foundation of China (Grant No. 12233010, 12173070, 11973010), and the Youth Innovation Promotion Association of the Chinese Academy of Sciences (Grant No. 2019265).

Author contributions XQX, MF and XHL performed the primary proposal of this manuscript. XQX and MF were the writers of this manuscript. YHZ calculated the AAM series. XQX finished the data processing.

Data availability The observed polar motion time series are from the International Earth Rotation and Reference System Service (IERS) website (https://www.iers.org/IERS/EN/DataProducts/EarthOrientationData/eop.html). The AAM are calculated based on the data from the National Center for Environmental Prediction/National Center for Atmospheric Research (NCEP/NCAR) reanalysis data set R1 (https://www.psl.noaa.gov/cdc/data.ncep.reanalysis.html); the coupled OAM data series are from Estimating the Circulation and Climate of the

Ocean (ECCO) (https://euler.jpl.nasa.gov/sbo/sbo_data.html). Another coupled AAM + OAM datasets are from Earth System Modeling GeoForschungsZentrum in Potsdam (ESMGFZ) (http://esmdata.gfz-potsdam.de:8080/).

Declarations

Conflict of interest The authors declare no conflict of interest.

References

Bizouard C (2020) Geophysical modelling of the polar motion. De Gruyter Stud Math Phys. https://doi.org/10.1515/9783110298093

Bizouard C, Remus F, Lambert S, Seoane L, Gambis D (2011) The Earth's variable Chandler Wobble. A&a 526:106. https://doi.org/10.1051/0004-6361/201015894

Bizouard C, Lambert S, Gattano C, Becker O, Richard JY (2019) The IERS EOP 14C04 solution for Earth orientation parameters consistent with ITRF 2014. J Geodesy 93:621–633. https://doi.org/10.1007/s00190-018-1186-3

Brzeziński A, Nastula J (2002) Oceanic excitation of the Chandler Wobble. Adv Space Res 2:195–200. https://doi.org/10.1016/S0273-1177(02)00284-3

Clark R (1985) Discrete polar motion equations. Geophys J Roy Astron Soc 80(2):551–554. https://doi.org/10.1111/j.1365-246X.1985.tb05109.x

Dill R, Dobslaw H, Thomas M (2019) Improved 90-day earth orientation predictions from angular momentum forecasts of atmosphere, ocean, and terrestrial hydrosphere. J Geodesy 93:287–295. https://doi.org/10.1007/s00190-018-1158-7

Dobslaw H, Dill R (2018) Predicting Earth orientation changes from global forecasts of atmosphere-hydrosphere dynamics. Adv Space Res 61:1047–1054. https://doi.org/10.1016/j.asr.2017.11.044

Fang M, Liao XH, Xu XQ (2021) On the Eigen-oscillator excitation of linear oscillators and the Earth's polar motion. Ann Phys 533:1–14

Fang M, Hager BF, Liao XH, Zhou YH, Xu XQ (2022) Revisit the theory of Earth rotation—anatomy of the Liouville equation. Geophys J Int 229(3):2175–2191. https://doi.org/10.1093/gji/ggac039

Gambis D (2004) Monitoring Earth orientation using space-geodetic techniques: state-of-the-art and prospective. J Geodesy 78:295–303. https://doi.org/10.1007/s00190-004-0394-1

Gibert D, Le Mouël JL (2008) Inversion of polar motion data: Chandler Wobble, phase jumps, and geomagnetic jerks. J Geophys Res. https://doi.org/10.1029/2008JB005700

Gross RS (1992) Correspondence between theory and observations of polar motion. Geophys J Int 109(1):162–170. https://doi.org/10.1111/j.1365-246X.1992.tb00086.x

Gross RS (2009) An improved empirical model for the effect of long-period ocean tides on polar motion. J Geod 83:635–644. https://doi.org/10.1007/s00190-008-0277-y

Gross RS, Fukumori I, Menemenlis D (2003) Atmospheric and oceanic excitation of the Earth's wobbles during 1980–2000. J Geophys Res. https://doi.org/10.1029/2002JB002143

Kalnay E et al (1996) The NCEP/NCAR 40-year reanalysis project. Bull Am Meteor Soc 77(3):437–471. https://doi.org/10.1175/1520-0477(1996)077%3c0437:TNYRP%3e2.0.CO;2

Malkin Z (2023) Revisiting recent amplitude and phase variations of the Chandler Wobble and free core nutation. Earth Planet Sci 2(2):33–37. https://doi.org/10.36956/eps.v2i2.873

Muskett RR (2021) GRACE, the Chandler Wobble and interpretations of terrestrial water transient storage. Int J Geosci 2:102–120. https://doi.org/10.4236/ijg.2021.122007

Nastula J, Salstein D (1999) Regional atmospheric angular momentum contributions to polar motion excitation. JGR 104(B4):7347–7358. https://doi.org/10.1029/1998JB900077

Nastula J, Salstein D, Kolaczek B (2009) Patterns of atmospheric excitation functions of polar motion from high-resolution regional sectors. JGR 114(4):2169–9313. https://doi.org/10.1029/2008JB005605

Nastula J, Salstein D, Gross R (2014) Regional multi-fluid-based geophysical excitation of polar motion. In: Proceedings of IAG general assembly 2011, Springer (2014): 467–472

Salstein DA, Rosen RD, Kann DM, Miller AJ (1993) The sub-bureau for atmospheric angular momentum of the international earth rotation service: a meteorological data center with geodetic applications. Bull Am Meteorol Soci 74:67–80. https://doi.org/10.1175/1520-0477(1993)074%3c0067:TSBFAA%3e2.0.CO;2

Seitz F, Schmidt M (2005) Atmospheric and oceanic contributions to Chandler Wobble excitation determined by wavelet filtering. J Geophys Res. https://doi.org/10.1029/2005JB003826

Smyliea DE, Henderson GA, Midhat Z (2015) Modern observations of the effect of earthquakes on the Chandler Wobble. J Geodyn 83:85–91. https://doi.org/10.1016/j.jog.2014.09.012

Wang GC et al (2016) Variable chandler and annual wobbles in Earth's polar motion during 1900–2015. Surv Geophys 37(6):1075–1093. https://doi.org/10.1007/s10712-016-9384-0

Wilson CR, Vicente RO (1990) Maximum likelihood estimates of polar motion parameters. Variat Earth Rotat 59:151–155. https://doi.org/10.1029/GM059p0151

Xu XQ, Zhou YH, Duan PS, Fang M, Kong ZY, Xu CC, An XR (2022) Contributions of oceanic and continental AAM to interannual variation in ΔLOD with the detection of 2020–2021 La Nina event. J Geod 96(6):1–10. https://doi.org/10.1007/s00190-022-01632-x

Xu XQ, Zhou YH, Xu CC (2023) Interannual variation in Earth's rotation rate and its role as a climate change indicator. Atmosphere. https://doi.org/10.3390/atmos14060982

Yamaguchi R, Furuya M (2024) Can we explain the post-2015 absence of the Chandler Wobble? Earth Planets Space 76:1. https://doi.org/10.1186/s40623-023-01944-y

Zhou YH, Zheng DW (1999) Monte carlo simulation tests of correlation significance levels. Acta Geodaetica Et Cartographica Sinica 28(4):313–319

Zhou YH, Chen JL, Liao XH (2005) Oceanic excitations on polar motion: a cross comparison among models. Geophys. J Int 162:390–398. https://doi.org/10.1111/j.1365-246X.2005.02694.x

Zotov LV, Bizouard C (2015) Regional atmospheric influence on the Chandler Wobble. Adv Space Res 55:1300–1306. https://doi.org/10.1016/j.asr.2014.12.013

Zotov LV, Bizouard C (2016) Reconstruction of prograde and retrograde Chandler excitation. J Inverse Ill-Posed Probl 24(1):99–105. https://doi.org/10.1515/jiip-2013-0085

Zotov LV, Sidorenkov NS, Bizouard C (2022) Anomalies of the Chandler Wobble in 2010s. Mosc Univ Phys Bull 77:555–563. https://doi.org/10.3103/S0027134922030134